



Improved magnetic properties and optimized preparation process of (MM)–Fe–B magnets

QIONG WU¹, HANGFU YANG¹, NENGJUN YU¹, MINXIANG PAN^{1,*}, CONG XIAN², PENGJIE ZHANG³, LIANG CHEN⁴, HONGWU YE⁵ and HONGLIANG GE¹

¹Magnetism Key Laboratory of Zhejiang Province, China Jiliang University, Hangzhou 310018, People's Republic of China

²The 9th Research Institute of China, Electronics Technology Group Corporation, Mianyang 621000, People's Republic of China

³BGRIMM Magnetic Materials and Technology Co. Ltd., Beijing 102600, People's Republic of China

⁴Dongyang Dingfeng Magnetics Co. Ltd., Jinhua 322100, People's Republic of China

⁵Zhejiang Fashion Institute of Technology, Ningbo 315000, People's Republic of China

*Author for correspondence (panminxiang@cjlu.edu.cn)

MS received 16 June 2023; accepted 16 August 2023

Abstract. Substitution of Nd element with misch metal (MM) element in the RE–Fe–B magnets has been set off as an effective method to decrease the cost of RE–Fe–B materials and ensure a more balanced utilization of rare-earth elements. In the present work, the composition of $\text{MM}_x\text{Fe}_{94-x}\text{B}_6$ ($x = 14$ and 16) alloys are fabricated by the melt-spinning method with wheel speeds of 20 and 25 m s^{-1} , respectively. It is demonstrated that with increasing wheel speed and MM content, can effectively suppress the formation of α -Fe soft phase and refine grain size. The maximum energy product $(BH)_{\text{max}}$ of 10.03 MGOe is obtained for the MM16-V25 alloy, which is a result of its higher intrinsic coercivity H_{cj} (H_{cj} : 9.15 kOe) and squareness H_k/H_{cj} (H_k/H_{cj} : 0.49). Meanwhile, the analysis of Henkel plots $\delta M(H)$ and microstructure show that the MM16-V25 alloy obtains the strongest exchange coupling effect and more uniform microstructure with fine grain size. In addition, the compositions of 2:14:1 grain and grain boundary from energy dispersive spectroscopy for the MM16-V25 alloy are also discussed in detail.

Keywords. Misch metal (MM); 2:14:1 phase; microstructure; Henkel plots.

1. Introduction

Re–Fe–B permanent magnet materials are widely used in the domains of network communication, aerospace, transportation, office automation, etc., due to their high maximum energy product, and have become one of the important material foundations for high-tech emerging industries and social progress [1–3]. Meanwhile, the extensive use of Re–Fe–B permanent magnet has led to excessive consumption of rare-earth elements Dy/Tb/Nd, as well as a large backlog of high abundance and low-cost rare-earth elements La/Ce/Y. This not only imbalances the utilization of rare-earth resources, but also increases the price of Re–Fe–B-based permanent magnets [4–6]. Therefore, the use of high abundance elements La/Ce instead of heavy rare-earth elements Dy/Tb/Nd to manufacture high-performance Re–Fe–B permanent magnet materials has become a hot research topic. So, if misch metal (MM) can be directly used to prepare high-performance Re–Fe–B magnets, it can effectively avoid the separation process of heavy rare-earth elements and greatly solve the problems of unbalanced

rare-earth use and environmental pollution, which will have great practical significance [7–10].

For Re–Fe–B magnetic materials based on MM, through the optimization of the composition and microstructure of MM–Fe–B, the performance of Re–Fe–B magnetic materials can be improved. Yu *et al.* [11] reported that the aggregation behaviour of La–Ce in the RE-rich grain boundary phase is beneficial to enhance the magnetic properties with high Curie temperature of $T_c = 502.9$ K. Zuo *et al.* [12] ultimately obtained 12 MGOe isotropic magnets in $\text{MM}_{13}\text{Fe}_{81}\text{B}_6$ alloys. Furthermore, Zhang *et al.* [13] demonstrated that optimizing melt-spinning cooling rates could control the grain size and finally enhance the magnetic properties of (La, Ce)–Fe–B ribbons. Therefore, it is desirable that the magnetic properties of MM–Fe–B magnets can be further enhanced by optimizing the alloy composition and manufacturing process.

In the present paper, the composition of $\text{MM}_x\text{Fe}_{94-x}\text{B}_6$ ($x = 14$ and 16) alloys with different wheel speeds (20 and 25 m s^{-1}) are fabricated by the melt-spinning method. The phase constituent, microstructure, magnetic properties and

Curie temperature of all the alloys are systematically investigated. Additionally, the relationships between the magnetic properties, demagnetization reversal behaviour, microstructure and exchange coupling interaction for the $\text{MM}_x\text{Fe}_{94-x}\text{B}_6$ alloys are discussed in detail.

2. Experimental

The ribbons with the nominal composition of $\text{MM}_x\text{Fe}_{94-x}\text{B}_6$ ($x = 14$ and 16) were fabricated by melt spinning under an Ar atmosphere. In the experiment, the purity information of raw materials includes Fe ($\geq 99.9\%$) and Fe-B (the content of B element is 20 wt%), while the MM with a purity of about 99.8 wt% from Bayan Obo mine. Then, the ribbon samples were produced by melt spinning with wheel speeds of 20 and 25 m s^{-1} , respectively. Meanwhile, the content of MM ($x = 14$) with wheel speed of 20 and 25 m s^{-1} , hereafter named as MM14-V20 and MM14-V25, respectively, while the content of MM ($x = 16$) with wheel speed of 20 and 25 m s^{-1} were marked as MM16-V20 and MM16-V25, respectively. X-ray diffraction (XRD) patterns of all the samples with the wheel surface were determined by the Empyrean S2 diffractometer (PANalytical Corporation, The Netherlands) by using the CuK_α radiation. Magnetic properties of the ribbons were obtained via the Lake Shore 7407 vibrating sample magnetometer (VSM) with a maximum applied field of 2 T. The magnetization-temperature (M - T) curves with the temperature range of 300–600 K under 1 T magnetic field and Henkel plots $\delta M(H)$ were also obtained via the VSM. The microstructure and microchemistry analyses of the ribbons were observed via the transmission electron microscope (TEM, Fei Techni F20) equipped with energy dispersive spectroscopy (EDS).

3. Results and discussion

XRD patterns of MM14-V20–MM16-V25 ribbons are presented in figure 1. The hard magnetic 2:14:1 phase (H) and the soft α -Fe phase (S) are observed in all the ribbons. The diffraction intensity of (110) plane of the soft α -Fe phase and the (214) plane of the hard 2:14:1 phase are marked as $I_{(110)S}$ and $I_{(214)H}$, respectively. According to the semi-quantitative technique, the peak intensity ratio of $I_{(110)S}/I_{(214)H}$ can estimate the relative volume fraction of the soft α -Fe phase and hard 2:14:1 phase in the alloys, and the calculation results of the peak intensity ratios $I_{(110)S}/I_{(214)H}$ are listed in table 1. It shows that the value of $I_{(110)S}/I_{(214)H}$ decreases gradually from 1.29 (MM14-V20) to 0.99 (MM16-V25), suggesting that the content of α -Fe phase decreases. Meanwhile, based on the data of XRD, table 1 provides refinement XRD data that displays the volume fraction and grain size of the MM14-V20–MM16-V25 alloys. It is found that the MM16-V25 alloy with a higher wheel speed and higher concentration of MM obtains

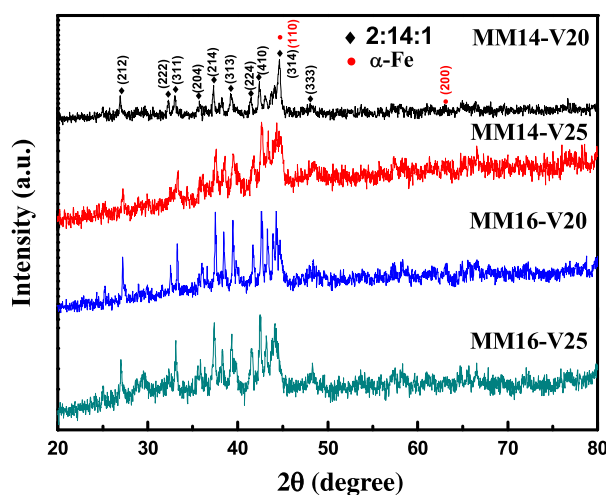


Figure 1. XRD patterns of the MM14-V20–MM16-V25 ribbons.

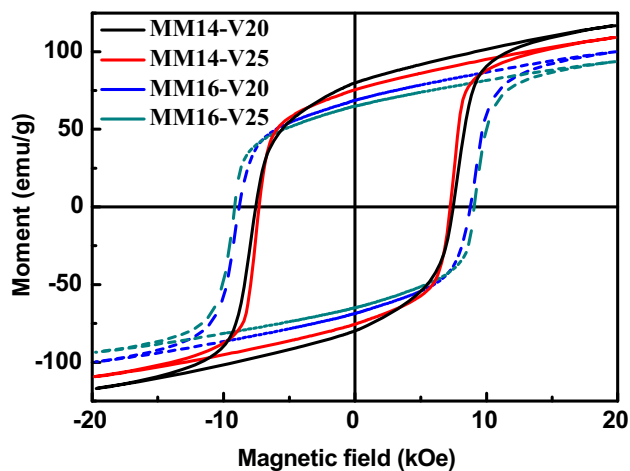
less volume fraction of the α -Fe phase ($V_{\alpha\text{-Fe}}$: $9.9 \pm 0.3\%$) and smaller grain size ($D_{2:14:1}$: 22 ± 1 nm, $D_{\alpha\text{-Fe}}$: 11 ± 2 nm), compared with MM14-V20 alloy ($V_{\alpha\text{-Fe}}$: $24.5 \pm 0.3\%$, $D_{2:14:1}$: 35 ± 2 nm, $D_{\alpha\text{-Fe}}$: 15 ± 1 nm). All the above results show that increasing wheel speed and MM content can effectively suppress the formation of the soft α -Fe phase and refine grain size. A similar result is also reported in the Nd-Fe-B alloys [14].

Figure 2 displays hysteresis loops of the MM14-V20–MM16-V25 ribbons at room temperature. The hysteresis loops of all the alloys display a single hard magnetic behaviour. Furthermore, the remanence M_r , intrinsic coercivity H_{cj} , squareness H_k/H_{cj} and the maximum energy product $(BH)_{\max}$ of the MM14-V20–MM16-V25 alloys are also illustrated in table 2. It shows that the remanence (M_r) of $\text{MM}_x\text{Fe}_{94-x}\text{B}_6$ alloys decreases gradually from 79.5 (MM14-V20) to 64.4 emu g^{-1} (MM16-V25), which is mainly caused by the reduction of soft α -Fe magnetic phase. In addition, the magnetic parameters of the squareness H_k/H_{cj} and the maximum energy product $(BH)_{\max}$ present a similar tendency that increase gradually. In conclusion, the optimal magnetic properties are obtained for the MM16-V25 alloy: $M_r = 64.4$ emu g^{-1} , $H_{cj} = 9.15$ kOe, $H_k/H_{cj} = 0.49$ and $(BH)_{\max} = 10.03$ MGOe. The enhanced $(BH)_{\max}$ value of the MM16-V25 alloy is a result of its higher intrinsic coercivity (H_{cj}) and squareness (H_k/H_{cj}) in the demagnetization curve, which can be attributed to its more refined microstructure. Furthermore, the Curie temperature T_c for the MM14-V20 and MM16-V25 samples is measured in the temperature range of 300–600 K under 1 T magnetic field (figure 3). It shows that the Curie temperature T_c of the MM14-V20 alloy is 495 K, which is close to the T_c of MM16-V25 (T_c : 500 K), indicating that the variation in MM rare-earth content has no significant effect on the Curie temperature of $\text{MM}_x\text{Fe}_{94-x}\text{B}_6$ alloys.

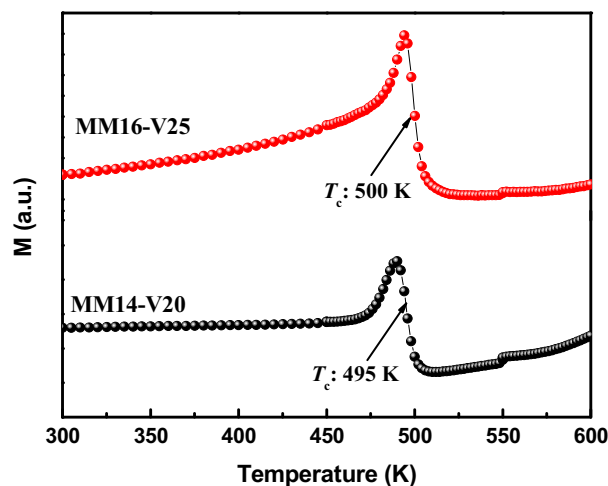
According to the above results, to further interpret the reason that the $\text{MM}_x\text{Fe}_{94-x}\text{B}_6$ alloys have higher magnetic properties, the Henkel plots, which are defined as follows

Table 1. Volume fraction and mean grain size of the MM14-V20–MM16-V25 alloys.

Alloys	Intensity ratio ($I_{(110)S}/I_{(214)H}$)	Volume fraction (%)		Mean grain size (nm)	
		2:14:1	α -Fe	2:14:1	α -Fe
MM14-V20	1.29	75.5 ± 0.4	24.5 ± 0.3	35 ± 2	15 ± 1
MM14-V25	1.15	85.5 ± 0.3	14.5 ± 0.3	27 ± 1	12 ± 2
MM16-V20	1.02	84.8 ± 0.2	15.2 ± 0.4	29 ± 2	13 ± 1
MM16-V25	0.99	90.1 ± 0.2	9.9 ± 0.3	22 ± 1	11 ± 2

**Figure 2.** Hysteresis loops of the MM14-V20–MM16-V25 ribbons at room temperature.

[15]: $\delta M(H) = [M_d(H) - M_r + 2M_r(H)]/M_r$, is an effective approach to analyse the exchange coupling among the hard magnetic 2:14:1 phase and the soft α -Fe phase. Here, $M_r(H)$ is the residual magnetism of a thermally demagnetized magnet after removing the external field under the action of a positive external magnetic field H . $M_d(H)$ is the residual magnetism of the sample after reaching saturation magnetization in the forward direction with the addition of a reverse field H and then removing the external field [16]. It is generally believed that positive value of $\delta M(H)$ characterizes the intergranular exchange coupling within the soft and hard magnetic phases, while negative value of $\delta M(H)$ is caused by dipole interaction [17]. As the grain size decreases to < 40 nm, an enhanced strong exchange coupling behaviour is observed among the soft and hard

**Figure 3.** M–T curves in the temperature range of 300–600 K under 1 T magnetic field for the MM14-V20 and MM16-V25 alloys.

magnetic grains [18,19]. Figure 4 shows the variation of $\delta M(H)$ curves with applied magnetic field for the MM14-V20–MM16-V25 ribbons. It shows that all the samples obtain one positive peak height value of δM at the reverse field, closely to the values of coercivity for each sample, suggesting that the existence of exchange coupled among soft and hard magnetic grains and a homogeneous magnetization reversal behaviour is acquired for the $MM_xFe_{94-x}B_6$ alloys. Evidently, the positive peak of the $\delta M(H)$ corresponding to MM16-V25 alloy is the highest, suggesting that this sample obtains stronger exchange coupling effect between the hard magnetic 2:14:1 phase and the soft α -Fe phase, and resulting in the highest maximum energy product.

Table 2. Remanence M_r , intrinsic coercivity H_{cj} , squareness H_k/H_{cj} and maximum energy product $(BH)_{max}$ of the MM14-V20–MM16-V25 alloys.

Alloys	M_r (emu g ⁻¹)	H_{cj} (kOe)	H_k/H_{cj}	$(BH)_{max}$ (MGOe)
MM14-V20	79.5	7.52	0.36	7.12
MM14-V25	75.1	7.28	0.42	8.36
MM16-V20	68.9	8.81	0.45	9.39
MM16-V25	64.4	9.15	0.49	10.03

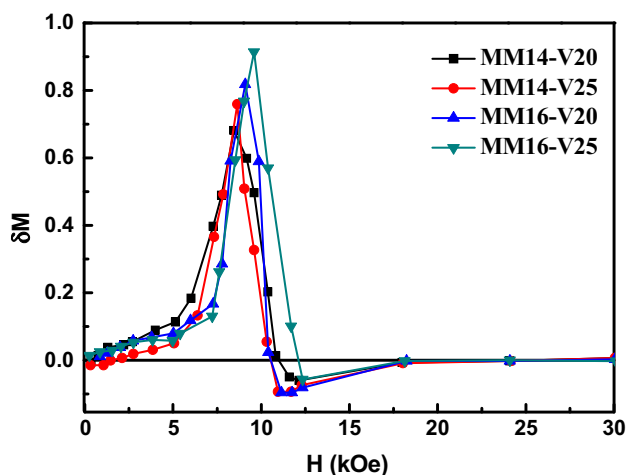


Figure 4. Variation of δM with applied magnetic field for the MM14-V20–MM16-V25 ribbons.

To further obtain the detailed nature of the structure, the TEM micrographs of the MM14-V20 and MM16-V25 alloys are performed in figure 5. One can see from figure 5a and b that a typical nanocrystalline structure can be observed. From figure 5a-1 and b-1 of the HRTEM images corresponding to red dotted line and the FFT diffraction pattern, it confirms that this grain (white regions) is corresponding to the 2:14:1 phase, while the white regions corresponding to yellow-dotted is α -Fe phase (figure 5a-2, b-2 and FFT diffraction pattern). Apparently, α -Fe grains for the two samples are both distributed between the 2:14:1 grains, suggesting the existence of exchange coupling interaction. Meanwhile, up to 40 grains are used to determine the average grain size, which is 36 nm for the MM14-V20 alloy, while the average grain size is reduced to 24 nm for the MM16-V25 alloy. These grain size results are compiled well with the estimates from previous XRD patterns, concluding that the MM16-V25 alloy with a higher wheel speed and

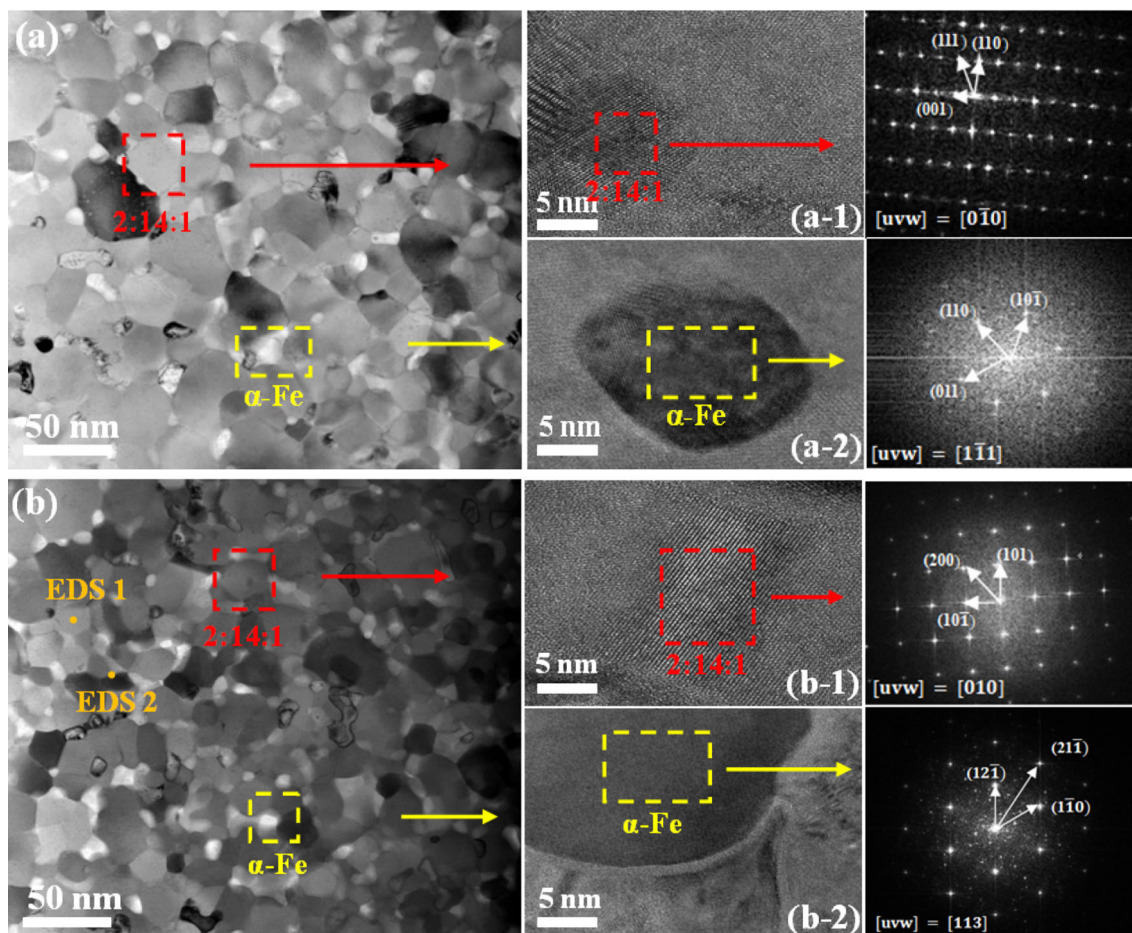


Figure 5. TEM micrographs of the MM14-V20 and MM16-V25 alloys. Bright-field images: (a) MM14-V20, (b) MM16-V25; HRTEM images of the 2:14:1 phase (a-1) and α -Fe phase (a-2) for the corresponding areas in (a). HRTEM images of the 2:14:1 phase (b-1) and α -Fe phase (b-2) for the corresponding areas in (b). The third column is the fast Fourier transform (FFT) diffraction patterns of the corresponding areas in (a-1), (a-2), (b-1) and (b-2).

Table 3. Compositions of 2:14:1 grain and grain boundary from EDS for the MM16-V25 alloy.

Element	EDS 1 (2:14:1 grain)		EDS 2 (grain boundary)	
	Composition (wt%)	Composition (at.%)	Composition (wt%)	Composition (at.%)
La	5.45	2.74	5.58	2.76
Ce	13.13	6.56	15.50	7.60
Pr	3.86	1.92	2.10	1.02
Nd	10.97	5.32	7.78	3.70
Fe	66.59	83.46	69.04	84.92

higher concentration of MM obtains smaller grain size. Therefore, compared with MM14-V20 sample, a more uniform microstructure and fine grain size are obtained for the MM16-V25 alloy with a higher wheel speed and higher concentration of MM, which is the reason for the enhanced magnetic properties in $MM_xFe_{94-x}B_6$ alloys.

To gain a further insight into the reason for the higher value of magnetic properties in the MM16-V25 alloy, the compositions of 2:14:1 grain (see the location of EDS 1 for figure 5b) and grain boundary (see the location of EDS 2 for figure 5b) from EDS for the MM16-V25 alloy are listed in table 3. It can be seen that La element is uniformly distributed and the composition of Pr and Nd elements is higher in the 2:14:1 grain, indicating that the Pr and Nd elements are more inclined to enter the 2:14:1 phase, while the Ce element is enriched in the grain boundary. Thus, the non-uniform distribution enables redundant Ce element to be enriched in grain boundary, resulting in a more favourable microstructure and enhanced magnetic properties. Similar element distribution characteristics have also been reported in Nd–La–Fe–B alloys [20].

4. Conclusion

In summary, the composition of $MM_xFe_{94-x}B_6$ ($x = 14$ and 16) alloys with different wheel speeds (20 and 25 m s^{-1}) are successfully prepared by melt-spinning technique. Meanwhile, the phase constituent, microstructure, magnetic properties and Curie temperature of all the alloys are systematically studied. The results indicate that the optimal magnetic characteristics are achieved in the MM16-V25 alloy: $M_r = 64.4 \text{ emu g}^{-1}$, $H_{cj} = 9.15 \text{ kOe}$, $H_k/H_{cj} = 0.49$ and $(BH)_{max} = 10.03 \text{ MGOe}$. The enhanced magnetic performance in the $MM_xFe_{94-x}B_6$ alloy may be attributed to the stronger exchange coupling effect and more uniform microstructure with fine grain size.

Acknowledgements

This work is supported by the National Key R&D Program of China (no. 2022YFB3504800), the National Natural

Science Foundation of China (no. 52271191), the Special Support Plan for High Level Talents of Zhejiang Province (no. 2022R52005), the Key R&D Program of Zhejiang Province (nos. 2021C01190 and 2021C01191) and the Key R&D Program of Ningbo City (no. 2021Z093).

References

- [1] Saramolee P, Lertsuriwat P, Hunyek A and Sirisathitkul C 2010 *Bull. Mater. Sci.* **33** 597
- [2] Zhou Y, Liu W, Zhao X G and Zhang Z D 2004 *J. Magn. Mater.* **278** 1
- [3] Yin W Z, Chen R J, Tang X, Ju J Y and Yan A R 2019 *J. Magn. Mater.* **482** 9
- [4] Liu Z W, Qian D Y, Zhao L Z, Zheng Z G, Gao X X and Ramanujan R V 2014 *J. Alloys Compd.* **606** 44
- [5] Kosobudskii I D, Sevost'yanov V P and Kuznetsov M Y 2000 *Inorg. Mater.* **36** 584
- [6] Liao X F, Zhang J S, Li W, Khan A J, Yu H Y, Zhong X C et al 2020 *J. Alloys Compd.* **834** 155226
- [7] Sugimoto S 2011 *J. Phys. D: Appl. Phys.* **44** 064001
- [8] Jin J, Ma T, Zhang Y, Bai G and Yan M 2016 *Sci. Rep.* **6** 32200
- [9] Skokov K P and Gutfleisch O 2018 *Scr. Mater.* **154** 289
- [10] Ito M, Yano M, Sakuma N, Kishimoto H, Manabe A, Shoji T et al 2016 *AIP Adv.* **6** 56029
- [11] Yu X Q, Yue M, Liu W Q, Li Z, Zhu M G and Dong S Z 2016 *J. Rare Earths* **34** 614
- [12] Zuo W L, Zuo S L, Li R, Zhao T Y, Hu F X, Sun J R et al 2017 *J. Alloys Compd.* **695** 1786
- [13] Zhang M, Li Z B, Shen B G, Hu F X and Sun J R 2015 *J. Alloys Compd.* **651** 144
- [14] Rehman S U, Jiang Q Z, He L K, Xiong H D, Liu K, Wang L et al 2019 *Phys. Lett. A* **383** 125878
- [15] Kelly P E, O'Grady K, Mayo P I and Chantrell R W 1989 *IEEE Trans. Magn.* **25** 3881
- [16] Wohlfarth E P 1958 *J. Appl. Phys.* **29** 595
- [17] Bollero A, Yan A, Gutfleisch O, Müller K H and Schultz L 2003 *IEEE Trans. Magn.* **39** 2944
- [18] Szmaja W, Grobelny J, Cichomski M, Hirosawa S and Shigemoto Y 2011 *Acta Mater.* **59** 531
- [19] Jiang Q Z, Lei W K, Zeng Q W, Quan Q C, Zhang L L, Liu R H et al 2018 *AIP Adv.* **8** 056203
- [20] Lei W K, Jiang Q Z, Rehman S U, He L K, Hu X J, Zeng Q W et al 2019 *J. Magn. Mater.* **473** 155